Three-photon-induced blue emission with narrow bandwidth from hot flower-like ZnO nanorods

Jun Dai,[1,2] Mao-Hui Yuan,[2] Jian-Hua Zeng,[2] Qiao-Feng Dai,[2] Sheng Lan,[2,*] Chai Xiao,[3] and Shao-Long Tie[3]

[1]*Research Center of Photoelectric Functional Materials and Devices, Guangdong Polytechnic Normal University, Guangzhou 510665, China*

[2]*Guangdong Provincial Key Laboratory of Nanophotonic Functional Materials and Devices, School of Information and Optoelectronic Science and Engineering, South China Normal University, Guangzhou 510006, China*

[3]*School of Chemistry and Environment, South China Normal University, Guangzhou 510006, China*

[*]*slan@scnu.edu.cn*

Abstract: ZnO nanorods (NRs) self-organized into flowers were synthesized at different temperatures ranging from 100°C to 180°C by using the hydrothermal method. The existence of Zn interstitials (Zn_i) was confirmed by X-ray photoelectron spectroscopy and a larger amount of Zn_i was found in the ZnO NRs prepared at higher temperatures. A redshift of the emission peak of more than 15 nm was observed for the ZnO NRs under single photon excitation. The nonlinear optical properties of the flower-like ZnO NRs were characterized by using focused femtosecond laser light and strong three-photon-induced luminescence was observed at an excitation wavelength of ~750 nm. More interestingly, a large redshift of the emission peak was observed with increasing excitation intensity, resulting in efficient blue emission with a narrow bandwidth of ~30 nm. It was confirmed that the large redshift originates from the heating of the ZnO NRs to a temperature of more than 800°C and the closely packed ZnO NRs in the flowers play a crucial role in heat accumulation. The stable and efficient three-photon-induced blue emission from such ZnO NRs may find potential applications in the fields of optical display, high-temperature sensors and light therapy of tumors.

©2015 Optical Society of America

OCIS codes: (160.6000) Semiconductor materials; (300.6170) Spectra; (190.4180) Multiphoton processes; (000.4930) Other topics of general interest.

References and links

1. D. M. Bagnall, Y. F. Chen, Z. Zhu, T. Yao, S. Koyama, M. Y. Shen, and T. Goto, "Optically pumped lasing of ZnO at room temperature," Appl. Phys. Lett. **70**(17), 2230–2232 (1997).
2. A. B. Djurisić and Y. H. Leung, "Optical properties of ZnO nanostructures," Small **2**(8-9), 944–961 (2006).
3. K. H. Tam, C. K. Cheung, Y. H. Leung, A. B. Djurisić, C. C. Ling, C. D. Beling, S. Fung, W. M. Kwok, W. K. Chan, D. L. Phillips, L. Ding, and W. K. Ge, "Defects in ZnO nanorods prepared by a hydrothermal method," J. Phys. Chem. B **110**(42), 20865–20871 (2006).
4. H. B. Zeng, G. T. Duan, Y. Li, S. K. Yang, X. X. Xu, and W. P. Cai, "Blue luminescence of ZnO nanoparticles based on non-Equilibrium processes: defect origins and emission controls," Adv. Funct. Mater. **20**(4), 561–572 (2010).
5. L. S. Panchakarla, A. Govindaraj, and C. N. R. Rao, "Formation of ZnO nanoparticles by the reaction of zinc metal with aliphatic alcohols," J. Cluster Sci. **18**(3), 660–670 (2007).
6. L. S. Panchakarla, M. A. Shah, A. Govindaraj, and C. N. R. Rao, "A simple method to prepare ZnO and Al $(OH)_3$ nanorods by the reaction of the metals with liquid water," J. Solid State Chem. **180**(11), 3106–3110 (2007).
7. M. Vafaee, M. Sasani Ghamsari, and S. Radiman, "Highly concentrated zinc oxide nanocrystals sol with strong blueemission," J. Lumin. **131**(1), 155–158 (2011).
8. W. K. Tan, G. Kawamura, H. Muto, K. A. Razak, Z. Lockman, and A. Matsuda, "Blue-emitting photoluminescence of rod-like and needle-like ZnO nanostructures formed by hot-water treatment of sol–gel derived coatings," J. Lumin. **158**(0), 44–49 (2015).

#250796 Received 28 Sep 2015; revised 26 Oct 2015; accepted 27 Oct 2015; published 30 Oct 2015
© 2015 OSA

9. S. Vempati, J. Mitra, and P. Dawson, "One-step synthesis of ZnO nanosheets: a blue-white fluorophore," Nanoscale Res. Lett. **7**(1), 470 (2012).
10. B. B. Jin and D. J. Wang, "Strong violet emission from zinc oxide dumbbell-like microrods and nanowires," J. Lumin. **132**(8), 1879–1884 (2012).
11. Z. Chen, X. X. Li, N. Chen, H. Wang, G. P. Du, and A. Y. M. Suen, "Effect of annealing on photoluminescence of blue-emitting ZnO nanoparticles by sol–gel method," J. Sol-Gel Sci. Technol. **62**(2), 252–258 (2012).
12. J. L. Zeng, X. W. Zhang, J. Z. Y. Tan, J. C. Bian, Z. Li, Z. D. Chen, R. Q. Peng, H. Y. He, J. Wang, and F. Yang, "Full-color photoluminescence of ZnO nanorod arrays based on annealing processes," J. Lumin. **135**(0), 201–205 (2013).
13. H. Zeng, W. Cai, P. Liu, X. Xu, H. Zhou, C. Klingshirn, and H. Kalt, "ZnO-based hollow nanoparticles by selective etching: elimination and reconstruction of metal-semiconductor interface, improvement of blue emission and photocatalysis," ACS Nano **2**(8), 1661–1670 (2008).
14. O. Mondal and M. Pal, "Strong and unusual violet-blue emission in ring shaped ZnO nanocrystals," J. Mater. Chem. **21**(45), 18354–18358 (2011).
15. S. K. Mishra, R. K. Srivastava, and S. G. Prakash, "ZnO nanoparticles: Structural, optical and photoconductivity characteristics," J. Alloys Compd. **539**(0), 1–6 (2012).
16. Q. Luo, L. S. Wang, H. Z. Guo, K. Q. Lin, Y. Chen, G. H. Yue, and D. L. Peng, "Blue luminescence from Ce-doped ZnO thin films prepared by magnetron sputtering," Appl. Phys., A Mater. Sci. Process. **108**(1), 239–245 (2012).
17. B. E. Urban, P. B. Neogi, S. J. Butler, Y. Fujita, and A. Neogi, "Second harmonic imaging of plants tissues and cell implosion using two-photon process in ZnO nanoparticles," J. Biophotonics **5**(3), 283–291 (2012).
18. S. K. Das, M. Bock, C. O'Neill, R. Grunwald, K. M. Lee, H. W. Lee, S. Lee, and F. Rotermund, "Efficient second harmonic generation in ZnO nanorod arrays with broadband ultrashort pulses," Appl. Phys. Lett. **93**(18), 181112 (2008).
19. J. I. Jang, S. Park, N. L. Frazer, J. B. Ketterson, S. Lee, B. K. Roy, and J. Cho, "Strong P-band emission and third harmonic generation from ZnO nanorods," Solid State Commun. **152**(14), 1241–1243 (2012).
20. S. K. Das, F. Güell, C. Gray, P. K. Das, R. Grunwald, and E. McGlynn, "ZnO nanorods for efficient third harmonic UV generation," Opt. Mater. Express **4**(4), 701–709 (2014).
21. S. Schmidt, M. Mascheck, M. Silies, T. Yatsui, K. Kitamura, M. Ohtsu, and C. Lienau, "Distinguishing between ultrafast optical harmonic generation and multi-photon-induced luminescence from ZnO thin films by frequency-resolved interferometric autocorrelation microscopy," Opt. Express **18**(24), 25016–25028 (2010).
22. R. Al-Gaashani, S. Radiman, A. R. Daud, N. Tabet, and Y. Al-Douri, "XPS and optical studies of different morphologies of ZnO nanostructures prepared by microwave methods," Ceram. Int. **39**(3), 2283–2292 (2013).
23. P. T. Hsieh, Y. C. Chen, K. S. Kao, and C. M. Wang, "Luminescence mechanism of ZnO thin film investigated by XPS measurement," Appl. Phys., A Mater. Sci. Process. **90**(2), 317–321 (2007).
24. D. Singh, A. A. Narasimulu, L. Garcia-Gancedo, Y. Q. Fu, T. Hasan, S. S. Lin, J. Geng, G. Shao, and J. K. Luo, "Vertically aligned smooth ZnO nanorod films for planar device applications," J. Mater. Chem. C Mater. Opt. Electron. Devices **1**(14), 2525–2528 (2013).
25. L. L. Yang, Q. X. Zhao, M. Willander, X. J. Liu, M. Fahlman, and J. H. Yang, "Origin of the surface recombination centers in ZnO nanorods arrays by X-ray photoelectron spectroscopy," Appl. Surf. Sci. **256**(11), 3592–3597 (2010).
26. O. Akhavan, M. Mehrabian, K. Mirabbaszadeh, and R. Azimirad, "Hydrothermal synthesis of ZnO nanorod arrays for photocatalytic inactivation of bacteria," J. Phys. D Appl. Phys. **42**(22), 225305 (2009).
27. J. P. S. Badyal, X. K. Zhang, and R. M. Lambert, "A model oxide catalyst system for the activation of methane: lithium-doped NiO on Ni(111)," Surf. Sci. **225**(1–2), L15–L19 (1990).
28. P. V. Kamath and C. N. R. Rao, "Electron spectroscopic studies of oxygen and carbon dioxide adsorbed on metal surfaces," J. Phys. Chem. **88**(3), 464–469 (1984).
29. T. Kawabe, S. Shimomura, T. Karasuda, K. Tabata, E. Suzuki, and Y. Yamaguchi, "Photoemission study of dissociatively adsorbed methane on a pre-oxidized SnO_2 thin film," Surf. Sci. **448**(2–3), 101–107 (2000).
30. L. Yu, X. X. Guo, and Y. X. Xu, "Effect of basicity and adding CO_2 in the feed on the oxidative coupling of methane over K_2O and SrO promoted La_2O_3/ZnO catalysts," Appl. Catal. A **164**(1–2), 47–57 (1997).
31. J. H. Zheng, Q. Jiang, and J. S. Lian, "Synthesis and optical properties of flower-like ZnO nanorods by thermal evaporation method," Appl. Surf. Sci. **257**(11), 5083–5087 (2011).
32. J. Das, S. K. Pradhan, D. R. Sahu, D. K. Mishra, S. N. Sarangi, B. B. Nayak, S. Verma, and B. Roul, "Micro-Raman and XPS studies of pure ZnO ceramics," Physica B **405**(10), 2492–2497 (2010).
33. G. R. Li, X. H. Lu, C. Y. Su, and Y. X. Tong, "Facile synthesis of hierarchical ZnO: Tb^{3+} nanorod bundles and their optical and magnetic properties," J. Phys. Chem. C **112**(8), 2927–2933 (2008).
34. M. Ahmad and J. Zhu, "ZnO based advanced functional nanostructures: synthesis, properties and applications," J. Mater. Chem. **21**(3), 599–614 (2011).
35. Y. C. Chang and L. J. Chen, "ZnO nanoneedles with enhanced and sharp ultraviolet cathodoluminescence peak," J. Phys. Chem. C **111**(3), 1268–1272 (2007).
36. W. G. Han, S. G. Kang, T. W. Kim, D. W. Kim, and W. J. Cho, "Effect of thermal annealing on the optical and electronic properties of ZnO thin films grown on p-Si substrates," Appl. Surf. Sci. **245**(1-4), 384–390 (2005).
37. D. Briggs and M. P. Seah, *Practical Surface Analysis by Auger and X-ray Photoelectron Spectroscopy* (John Wiley & Sons, 1983).
38. M. A. Arenas, I. García, and J. de Damborenea, "X-ray photoelectron spectroscopy study of the corrosion behaviour of galvanised steel implanted with rare earths," Corros. Sci. **46**(4), 1033–1049 (2004).

#250796 Received 28 Sep 2015; revised 26 Oct 2015; accepted 27 Oct 2015; published 30 Oct 2015
© 2015 OSA

39. C. Rameshan, C. Weilach, W. Stadlmayr, S. Penner, H. Lorenz, M. Hävecker, R. Blume, T. Rocha, D. Teschner, A. Knop-Gericke, R. Schlögl, D. Zemlyanov, N. Memmel, G. Rupprechter, and B. Klötzer, "Steam reforming of methanol on PdZn near-surface alloys on Pd (111) and Pd foil studied by in-situ XPS, LEIS and PM-IRAS," J. Catal. **276**(1), 101–113 (2010).
40. A. B. Djurišić, W. C. H. Choy, V. A. L. Roy, Y. H. Leung, C. Y. Kwong, K. W. Cheah, T. K. R. Rao, W. K. Chan, H. F. Lui, and C. Surya, "Photoluminescence and electron paramagnetic resonance of ZnO tetrapod structures," Adv. Funct. Mater. **14**(9), 856–864 (2004).
41. W. S. Shi, B. Cheng, L. Zhang, and E. T. Samulski, "Influence of excitation density on photoluminescence of zinc oxide with different morphologies and dimensions," J. Appl. Phys. **98**(8), 083502 (2005).
42. Z. W. Liang, X. Yu, B. F. Lei, P. Y. Liu, and W. J. Mai, "Novel blue-violet photoluminescence from sputtered ZnO thin films," J. Alloys Compd. **509**(17), 5437–5440 (2011).
43. H. B. Zeng, Z. G. Li, W. P. Cai, and P. S. Liu, "Strong localization effect in temperature dependence of violet-blue emission from ZnO nanoshells," J. Appl. Phys. **102**(10), 104307 (2007).
44. P. Zijlstra, J. W. M. Chon, and M. Gu, "Effect of heat accumulation on the dynamic range of a gold nanorod doped polymer nanocomposite for optical laser writing and patterning," Opt. Express **15**(19), 12151–12160 (2007).
45. R. Hauschild, H. Priller, M. Decker, J. Brückner, H. Kalt, and C. Klingshirn, "Temperature dependent band gap and homogeneous line broadening of the exciton emission in ZnO," Phys. Status Solidi **3**(4), 976–979 (2006).
46. V. V. Ursaki, I. M. Tiginyanu, V. V. Zalamai, E. V. Rusu, G. A. Emelchenko, V. M. Masalov, and E. N. Samarov, "Multiphonon resonant Raman scattering in ZnO crystals and nanostructured layers," Phys. Rev. B **70**(15), 155204 (2004).
47. S. G. S. Beirão, A. P. C. Ribeiro, M. J. V. Lourenço, F. J. V. Santos, and C. A. Nieto de Castro, "Thermal conductivity of humid air," Int. J. Thermophys. **33**(8-9), 1686–1703 (2012).

1. Introduction

As a semiconductor with wide band gap (3.37 eV) and large exciton binding energy (60 meV), ZnO has attracted great interest in the last two decades due to its potential applications in various fields of science and technology [1,2]. With the rapid development in synthesis method and characterization technique, ZnO nanomaterials in different fashions have been intensively and extensively investigated owing to their unique optical, electronic, thermotic, magnetic, and acoustic properties and much attention has been paid to ZnO nanowires or nanorods (NRs) that exhibit many interesting physical properties and great potential in practical application. This kind of one-dimensional nanomaterials is considered as a potential candidate for making sophisticated optoelectronic devices. As compared to their electronic properties, the optical properties of ZnO NRs have attracted more attention. Due to their good optical properties, avirulence and biological compatibility, the emission of ZnO nanomaterials would have potential applications in the fields of visible light emitting devices, biological imaging and light therapy of tumors. However, most of the previous studies focus on the excitonic emission of ZnO nanomaterials which generally appears as violet light. In comparison, less attention has been paid to the control and engineering of the emission originating from the defects intentionally introduced in ZnO nanomaterials. It has been confirmed that the optical properties, especially the emission properties of ZnO NRs, are closely related to the intrinsic and extrinsic defects introduced into ZnO NRs [3]. By appropriately controlling these defects, one can create rich energy levels covering the whole visible light region. In particular, the control and engineering of such defect levels is highly desirable for the applications such as light-emitting devices and optical sensors. In most cases, the emission of ZnO NRs is dominated by either the violet emission originating from the radiative recombination of excitons or by the green emission arising from the defect levels of oxygen vacancies (V_O). In contrast, the observation of blue emission from ZnO nanomaterials is quite rare because the formation energy of Zn interstitials (Zn_i), whose emission appears in the violet or blue region, is much larger than that of V_O. It has been shown that the defect levels related to Zn_i can be introduced into ZnO nanoparticles fabricated in a nonequilibrium condition [4–7]. So far, the blue emissions reported for ZnO nanostructures are generated mainly by using single photon excitation and they usually possess broad bandwidths and weak intensities [8–16]. In recent years, the nonlinear optical responses of ZnO nanomaterials have become the focus of many studies because of their potential applications in the field of biophotonics where the use of laser light in the near infrared region is preferred in order to avoid the damage of living tissue. By using

#250796 Received 28 Sep 2015; revised 26 Oct 2015; accepted 27 Oct 2015; published 30 Oct 2015
© 2015 OSA

femtosecond (fs) laser excitation, the nonlinear optical responses such as second and third harmonic generation (SHG [17,18] and THG [19,20]) and multiphoton-induced luminescence (MPL [21]) have been demonstrated in various ZnO nanomaterials. However, the blue emission from ZnO NRs induced by multiphoton excitation remains unexplored. It is considered that the efficient multiphoton-induced blue emission from ZnO NRs can be realized by utilizing and controlling the Zn_i in ZnO NRs.

So far, ZnO NRs have been successfully synthesized by using different physical and chemical methods. The morphology of ZnO NRs and the defects introduced in ZnO NRs depend strongly on synthesis method and experimental condition. For wet chemical methods such as chemical coprecipitation and hydrothermal methods, soft templates such as polyethylene glycol (PEG), cetyltrimethyl ammonium bromide (CTAB) and triethanolamine (TEA) were generally employed in order to obtain appropriate ZnO NRs. These methods generally take a long time (e.g., more than ten hours) and lead to a low concentration of Zn_i. It has been confirmed that an environment with low-pressure oxygen or reduction atmosphere is helpful for the formation of Zn_i. However, the homogeneous distribution of Zn_i inside ZnO NRs cannot be achieved by using such methods because of the acute activity of zero-valence Zn atoms. Therefore, a quick method for synthesizing ZnO NRs is necessary in order to achieve stable Zn_i with a large concentration.

In this article, we report on the synthesis of Zn_i-rich ZnO NRs by using a fast hydrothermal method in which three soft templates (PEG, CTAB and TEA) were employed. The as-prepared ZnO NRs were self-organized into flowers in which NRs were closely packed. In addition, the concentration of Zn_i was found to increase with increasing synthesis temperature. A redshift of the emission peak of more than 15 nm was found for the ZnO NRs under single photon excitation. In addition, a strong blue emission band with a narrow bandwidth of ~30 nm was observed when irradiating the ZnO NRs with focused fs laser light at 750 nm. By analyzing the dependence of the luminescence intensity on the excitation intensity, it was revealed that the luminescence was composed of the emissions from the excitons and Zn_i following the three-photon-induced absorption (3PA). The blue emission originated from the cooperation of the three-photon-induced luminescence (3PL) and the significant heat accumulation effect existing in the flower-like ZnO NRs.

2. Experimental detail and numerical method

In our experiments, all chemicals (A.R. in purity) were used as received without further purification and deionized water was used throughout the whole experiment. Typically, 0.006 mol $Zn(NO_3)_2 \cdot 6H_2O$ and 0.03 mol NaOH were dissolved in 7.5 mL deionized water, adding 0.006 mol TEA. Then, 4g PEG-2000 was dissolved in a mixed solvent composed of 50 mL anhydrous ethanol and 10 mL deionized water, adding 0.01 mol CTAB. Finally, the above two solutions were mixed and moved into a high-pressure Teflon-lined autoclave for one-hour hydrothermal treatment at different temperatures of 373, 393, 413, 433, and 453 K, corresponding to 100, 120, 140, 160, and 180°C, respectively. After the reaction, the autoclave was cooled down naturally to room temperature. The white suspension was collected by using a suction filter and washed thoroughly with absolute alcohol and hot water for three times, drying in air at 60°C for one hour.

The X-ray diffraction (XRD) patterns of the as-prepared samples were examined by using an X-ray powder diffractometer (AXS D8-Advance, Bruker). Their morphology was characterized by using field emission scanning electron microscope (FE-SEM) (Ultra 55, Zeiss) equipped with an energy dispersive spectroscopy (EDS) and high resolution transmission electron microscope (HR-TEM) (JEM-2100, JEOL). The absorption spectra in the spectral region of ultraviolet to near infrared were measured by using a photometer (Cary 5000, Varian) while the photoluminescence (PL) spectra were measured by using a PL spectrometer (F-4500, Hitachi). The combination of an inverted microscope (Observer A1, Zeiss) with a Ti:sapphire fs laser (Mira 900S, Coherent) was employed to characterize the nonlinear optical properties of the as-prepared samples. The excitation intensity was characterized by the peak power density of the fs laser pulses. The temperature distribution

#250796 Received 28 Sep 2015; revised 26 Oct 2015; accepted 27 Oct 2015; published 30 Oct 2015
© 2015 OSA

and the heat accumulation effect inside the flower-like ZnO NRs were simulated by using a commercial software (ANSYS, http://www.ansys.com).

3. Results and discussion

3.1Morphology of the ZnO NRs

The SEM images of the ZnO NRs prepared at different temperatures are shown in Fig. 1. In all samples, we observed flower-like ZnO NRs whose length increases with increasing temperature. The ZnO NRs synthesized at low temperatures were found to have ends with regular hexagonal prisms while those prepared at high temperatures have ends with regular hexagonal pyramids. The regular hexagonal pyramid and side structure correspond to the crystallographic facets (101) and (100) identified in the XRD patterns, as shown in Fig. 2. For comparison, the SEM image of the ZnO NRs synthesized by using the coprecipitation method is also provided [see Fig. 1(f)].

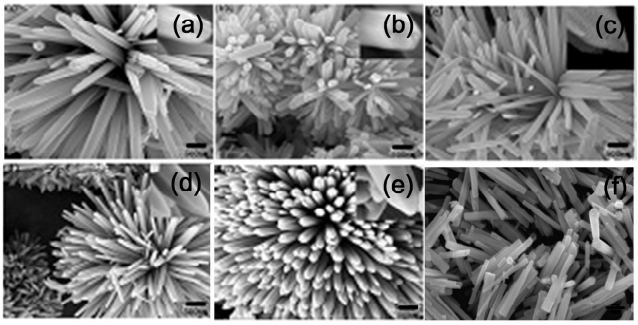

Fig. 1. SEM images of the ZnO NRs prepared by using the hydrothermal method at different temperatures of (a) 100°C, (b) 120°C, (c) 140°C, (d) 160°C and (e) 180°C and the coprecipitation method at 180°C (f). The length of the scale bar is 0.5 μm.

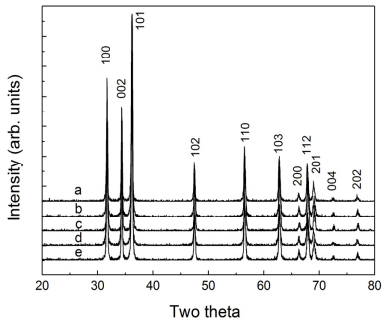

Fig. 2. XRD patterns measured for the ZnO NRs synthesized at different temperatures. (a) 100°C, (b) 120°C, (c) 140°C, (d) 160°C, and (e) 180°C.

3.2 PL spectra of the ZnO NRs under single photon excitation

Under single photon excitation at 325 nm, the PL spectra of the ZnO NRs synthesized at different temperatures exhibit broad emission bands in the visible spectral region, as shown in Fig. 3. In general, the emission of undoped ZnO nanomaterials is related to various intrinsic defects introduced in the fabrication process. Typical defects include Zn interstitials (Zn_i) and Zn and O vacancies (V_{Zn} and V_O) which act as donors and acceptors, respectively. The electronic transitions between the defect levels and the conduction/valence bands of ZnO give rise to various emissions in the visible spectral region. The identification of such electronic transitions relies on not only the matching of the energy interval with the emission wavelength but also other evidences indicating the existence of the corresponding defects.

#250796 Received 28 Sep 2015; revised 26 Oct 2015; accepted 27 Oct 2015; published 30 Oct 2015
© 2015 OSA

In Fig. 3, one can see an emission peak at ~400 nm with two shoulders at ~385 and ~420 nm for the ZnO NRs prepared at 100°C. As compared with the ZnO NRs prepared via the coprecipitation method, the emission peak is red shifted by ~15 nm. The emission originating from free excitons, which generally appears at 385 nm, is degenerated as a shoulder. For the ZnO NRs prepared at 120°C and 140°C, the relative intensity of the shoulder located 385 nm decreases while that of the shoulder located at ~420 nm increases. A further decrease of the former as well as a rapid increase of the latter is observed for the ZnO NRs prepared at 160°C and 180°C. As a result, the emission peak appears at ~417 nm. In all samples, the broad emission band centered at ~550 nm, which is related with V_O, was not observed, implying the low content of V_O in the ZnO NRs. The redshift of the emission peak is attributed to the bandgap renormalization induced by the large concentration of Zn_i which act as shallow donors in ZnO. The evolution of the PL spectrum indicates the increase in the concentration of Zn_i with increasing synthesis temperature.

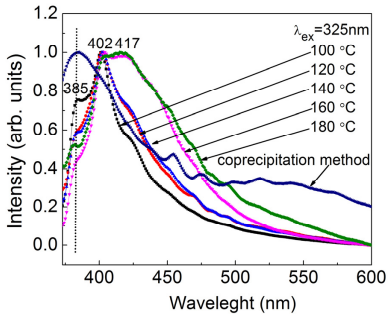

Fig. 3. Normalized PL spectra under the 325-nm excitation for the ZnO NRs synthesized at different temperatures. The PL spectrum of the ZnO NRs prepared by using the coprecipitation method is also provided for comparison.

3.3 Chemical states of Zn and O in the ZnO NRs

In order to understand the chemical states of elements Zn and O in the ZnO NRs and the effects of synthesis temperature on the formation of defects, we examined the X-ray photonelectron spectroscopy (XPS) spectra of the ZnO NRs prepared at 100°C, 140°C, and 180°C. As an example, the survey scan spectrum for the ZnO NRs prepared at 180°C is shown in Fig. 4 and the magnified XPS spectra related to the states of O 1s, Zn 2p, and Zn LMM are presented in the following.

In Fig. 4, the main peaks corresponding to C 1s, Zn 3d, Zn 3p, Zn 3s, O 1s, Zn LMM, and Zn 2p are marked. After calibration by using the peak of C 1s (284.5 eV), the peak positions of other states are in good agreement with those reported previously for ZnO NRs [22–26]. No peaks corresponding to other elements were observed in the XPS spectrum, indicating the high purity of the ZnO NRs.

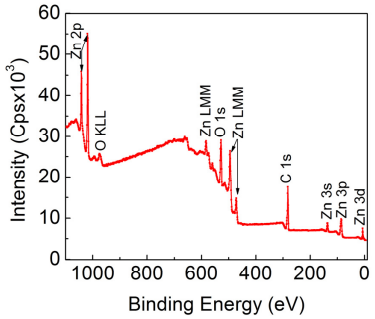

Fig. 4. Survey scan XPS spectrum for the ZnO NRs prepared at 180°C.

#250796 Received 28 Sep 2015; revised 26 Oct 2015; accepted 27 Oct 2015; published 30 Oct 2015
© 2015 OSA

As shown in Fig. 5, the magnified XPS spectra of O 1s for the ZnO NRs prepared at 100°C, 140°C and 180°C can be fitted by using two or three Gaussian peaks corresponding to the binding energies of O atoms on the surfaces of the ZnO NRs. For the ZnO NRs prepared at 100°C, only two peaks located at 529.5 and 531.3 eV are observed and they are attributed to the peaks of lattice O in ZnO and O in M-OH or chemisorbed water [25]. For the ZnO NRs prepared at 140°C and 180°C, a new peak located at 532.7 eV is observed. This peak is attributed to molecularly chemisorbed O_2^{2-} species which has been observed previously in SnO_2, nickel, and copper with slightly different energies of 532.6 eV, 532.7 eV and 533 eV [26–30], indicating the formation of Zn_i. It is noticed that the intensity of the peak becomes larger in the ZnO NRs prepared at 180°C, implying an increase of Zn_i with increasing synthesis temperature. Since the signals obtained in the XPS measurements reflect the content of a certain element near the surfaces of the ZnO NRs, we can conclude that the content of O 1s, which represents hydroxyl or chemisorbed water, decreases with increasing synthesis temperature. This result was further verified by the Fourier transform infrared spectra measured for the three samples, as shown in Fig. 6. The transmission valleys appearing in the wavelength range of 3100–3500 cm^{-1} represent the absorption peaks related to hydroxyl and their intensities decrease with increasing synthesis temperature. It is consistent with the fact that in hydrothermal conditions the contents of –OH and chemisorbed water are reduced with increasing temperature and pressure.

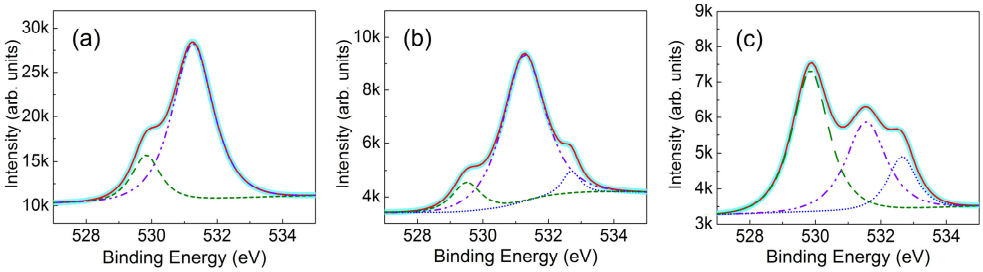

Fig. 5. Comparison of the XPS spectra of O 1s in the ZnO NRs prepared at (a) 100°C, (b) 140°C, and (c) 180°C. The thick solid curves are the measured spectra while the thin solid curves, the dashed curves, and the dot-dashed curves are the Gaussian fittings of the spectra.

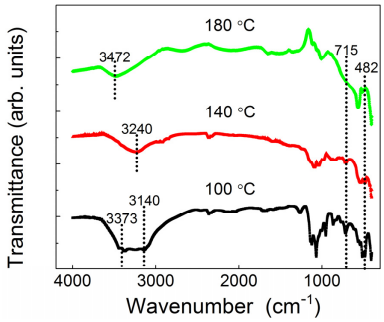

Fig. 6. Fourier transform infrared spectra measured for the ZnO NRs synthesized at different temperatures. For clarity, the spectra are vertically shifted.

#250796 Received 28 Sep 2015; revised 26 Oct 2015; accepted 27 Oct 2015; published 30 Oct 2015
© 2015 OSA

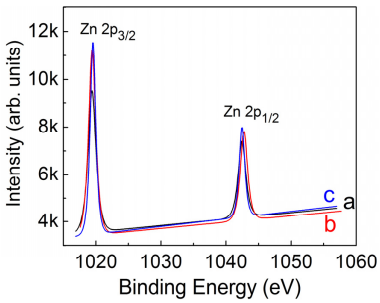

Fig. 7. XPS spectra of Zn 2p in the ZnO NRs prepared at different temperatures of (a) 100°C, (b) 140°C, and (c) 180°C.

The XPS spectra of Zn 2p for the three samples are presented in Fig. 7 where two peaks located at 1021.5eV (Zn $2p_{3/2}$) and 1044.5eV (Zn $2p_{1/2}$) are observed. The spin–orbit splitting energy (23.0 eV) derived from the binding energies of Zn $2p_{3/2}$ and Zn $2p_{1/2}$ is in good agreement with that reported for Zn^{2+} in ZnO [31–33]. However, the binding energies of Zn $2p_{3/2}$ and Zn $2p_{1/2}$ are found to shift to lower energies as compared with the values reported in previous literature [33,34], indicating a change in the chemical environment surrounding Zn atoms. For example, more O atoms are bound to Zn atoms (including Zn_i) in form of chemisorbed O_2^{2-} [35,36], as confirmed later by the XPS spectra of Zn LMM.

In fact, the valence of Zn in the ZnO NRs can be determined by the Auger signals of Zn $L_3M_{4,5}M_{4,5}$ or Zn LMM, as shown in Fig. 8 for the three samples. By using Gaussian fitting, two peaks located at 987.9 and 990.2 eV are observed for the ZnO NRs prepared at 100°C, as shown in Fig. 8(a). Differently, three Gaussian peaks located at 984.9, 989.2 and 992.2 eV are observed for the ZnO NRs prepared at 140°C while three Gaussian peaks are observed at 989.2, 990.7 and 992.7 eV for the ZnO NRs prepared at 180°C, as can be seen in Figs. 8(b) and 8(c). Comparing with the Zn LMM peak reported for pure metal Zn (Zn^0, zinc with zero valence) which appears at 992.5 eV and that reported for ZnO (Zn_{OX}, zinc with oxidation) which appears at 988.2 eV [37,38], the peak observed at ~992 eV for the ZnO NRs prepared at 140°C and 180°C is attributed to Zn^0. As far as we know, this is the first time to observe Zn^0 in ZnO NRs. It is noticed that the intensity of the peak at ~992 eV becomes larger in the ZnO NRs prepared at 180°C, implying a larger concentration of Zn^0 on the surfaces of ZnO NRs [39]. Actually, the increase of Zn_i^0 with increasing temperature is also reflected in the PL spectra shown in Fig. 3 where a redshift of the emission peak to ~420 nm is observed in the ZnO NRs synthesized at high temperatures (160°C and 180°C).

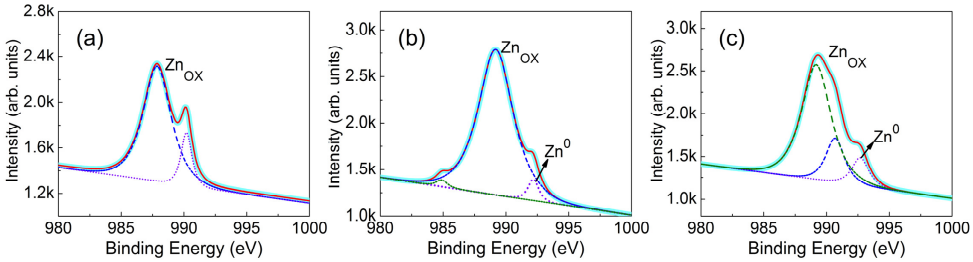

Fig. 8. Auger signals of Zn LMM measured for the ZnO NRs prepared at different temperatures of (a) 100°C, (b) 140°C, and (c) 180°C. The thick solid curves are the measured spectra while the thin solid curves, the dashed curves, and the dot-dashed curves are the Gaussian fittings of the spectra.

3.4 Nonlinear optical properties of the ZnO NRs

Having known that Zn_i is introduced in the fabrication process of the ZnO NRs and the concentration of Zn_i is larger in the ZnO NRs synthesized at high temperatures, let's examine

#250796 Received 28 Sep 2015; revised 26 Oct 2015; accepted 27 Oct 2015; published 30 Oct 2015
© 2015 OSA

the effects of Zn_i on the linear and nonlinear optical properties of the ZnO NRs. In Fig. 3, we have shown that the PL peak of the ZnO NRs prepared by using the hydrothermal method appears in the region of 400–417 nm, depending strongly on the synthesis temperature. In comparison, the PL peak of the ZnO NRs prepared by using the coprecipitation method appears at ~385 nm. This behavior is easily understood because Zn_i act as shallow donors in ZnO. The bandgap energy of the ZnO NRs is expected to be reduced due to the existence of Zn_i with a large concentration.

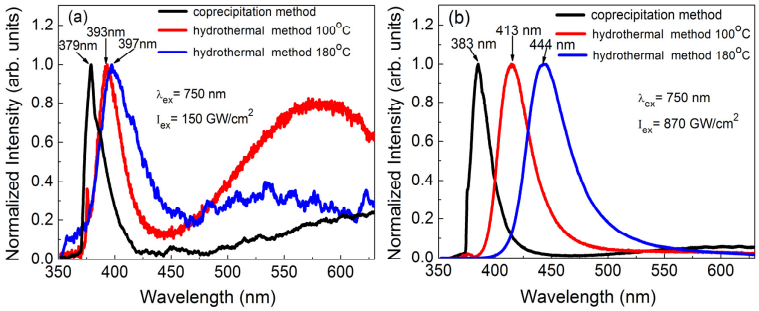

Fig. 9. Comparison of the MPL spectra of the ZnO NRs prepared by using the hydrothermal method at 100°C and 180°C and the coprecipitation method at 180°C.

Apart from the luminescence induced by single photon excitation, it has been shown that MPL can also be observed in ZnO films or nanoparticles by using a fs laser with a high repetition rate. In our experiments, the combination of a fs laser with a microscope enables the achievement of extremely high excitation intensity which is quite useful for studying MPL. In Fig. 9, we compare the nonlinear response spectra of the ZnO NRs prepared by using different methods. The excitation wavelength was chosen to be 750 nm. Under a low excitation intensity of 150 GW/cm^2, the MPL peak of the ZnO NRs prepared by the coprecipitation method appears at ~379 nm while that of the ZnO NRs prepared by the hydrothermal method appears at ~395 nm, as shown in Fig. 9(a). Under a high excitation intensity of 870 GW/cm^2, the MPL peak of the ZnO NRs prepared by the coprecipitation method is slightly shifted to ~383 nm. In contrast, the MPL peak of the ZnO NRs synthesized by the hydrothermal method at 100°C is largely shifted to ~413 nm while that synthesized at 180 °C is significantly shifted to ~444 nm, as can be seen in Fig. 9(b).

The evolution of the nonlinear response spectrum with increasing excitation intensity measured for the ZnO NRs synthesized by using the hydrothermal method at 180°C is shown in Fig. 10. The excitation wavelength was chosen to be 750 nm. In each case, the photo for the excitation spot taken from the eyepiece of the microscope is also provided as an inset.

#250796 Received 28 Sep 2015; revised 26 Oct 2015; accepted 27 Oct 2015; published 30 Oct 2015
© 2015 OSA

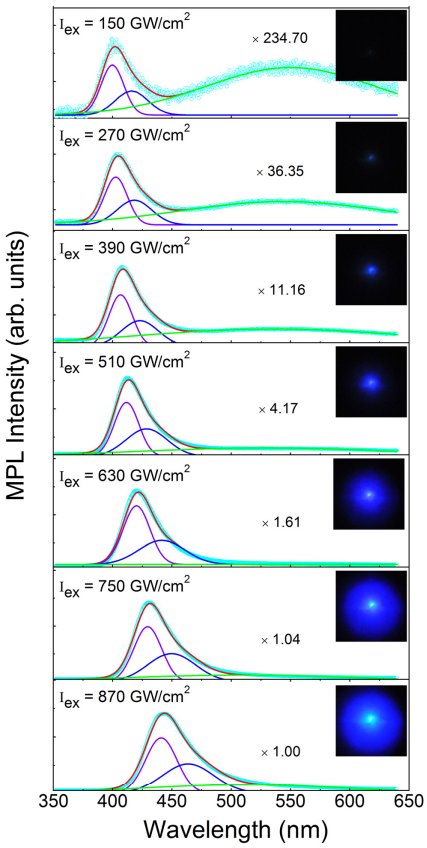

Fig. 10. Evolution of the MPL spectrum with increasing excitation intensity for the ZnO NRs prepared 180°C. At each excitation intensity, the fitting of the spectrum with multiple Gaussian peaks is presented. The inset shows the photo of the excitation spot taken from the eyepiece of the microscope.

As shown in Fig. 10, the most important feature of the excitation-intensity-dependent MPL is the large redshift of the emission peak wavelength from ~400 nm (violet) to ~445 nm (blue), which is accompanied with the dramatic increase in the MPL intensity. At the highest excitation intensity we used (870 GW/cm^2), blue emission with a narrow bandwidth of ~30 nm is observed. In order to clearly understand the physical mechanism responsible for the excitation-intensity-dependent MPL from the ZnO NRs, the PL spectra were decomposed by using multiple Gaussian fitting. At the lowest excitation intensity of 150 GW/cm^2, the spectrum can be decomposed into three emission bands centered at 400, 415, and 550 nm, respectively. They are attributed to the emissions from the free excitons, Zn_i, and V_O, respectively. It is noticed that the emission from the free excitons is red shifted to ~400 nm as compared with that of undoped ZnO nanomaterials which generally appears at 385 nm. The redshift of the emission wavelength originates from the bandgap renormalization induced by the large concentration of Zn_i that act as shallow donors in ZnO. In Fig. 10, it can be seen that the contribution of the green emission band from V_O becomes negligible at high excitation densities as compared with the other two emission bands. Therefore, we will focus only on the evolution of the first two emission bands (from the free excitons and Zn_i) with increasing excitation intensity. The evolution of the peak intensity, peak wavelength and bandwidth with increasing excitation intensity for the first two emission bands are compared in Figs. 11(a), 11(b) and 11(c), respectively.

For undoped ZnO films and nanomaterials fabricated by different methods, the PL is generally dominated by the green emission band related to V_O no matter single photon

#250796 Received 28 Sep 2015; revised 26 Oct 2015; accepted 27 Oct 2015; published 30 Oct 2015
© 2015 OSA

excitation or multiphoton excitation is employed. In addition, the relative intensities of the free excitons and defect emission are dependent on the excitation intensity and the excitation area [40,41]. So far, there have been some reports on the blue emission from ZnO nanomaterials induced by single photon excitation, such as the ZnO nanoparticles fabricated in a non-equilibrium environment (e.g., laser ablation-induced extreme conditions and zinc-rich annealing). It has been suggested that Zn_i are responsible for the blue emission [4,7,9,11,42,43]. However, the emission spectra observed previously usually possess a broad bandwidth of ~150 nm or more, indicating that the energy levels related to different defects are involved in the generation of blue emission. In contrast to the blue emission generated by single photon excitation, the observation of blue emission from ZnO nanomaterials by using multiphoton excitation is very rare. To the best of our knowledge, there is no report on the multiphoton-induced blue emission with a narrow bandwidth from ZnO NRs, which is quite important for the applications in biophotonics where the single photon excitation by using violet light is not preferred.

3.5 Physical mechanism for the redshift of the MPL

So far, some physical mechanisms have been proposed to explain the blue emission observed in ZnO nanomaterials. Since the electronic transition from the defect levels of Zn_i to the valence band appears in the violet region, the blue emission is usually suggested to be the electronic transition from the defect levels of Zn_i to the energy levels of some shallow acceptors or from the extended states of Zn_i with a lower energy to the valence band when the content of Zn_i is large [4]. Based on the hydrothermal method we used to synthesize the flower-like ZnO NRs, it is expected that a large amount of Zn_i will be introduced in the fabrication process and the emission from Zn_i will play an important role in the generation of MPL. The existence of Zn_i is confirmed by the XPS measurements for the ZnO NRs synthesized at different temperatures. A larger concentration of Zn_i was found in the ZnO NRs obtained at higher temperatures.

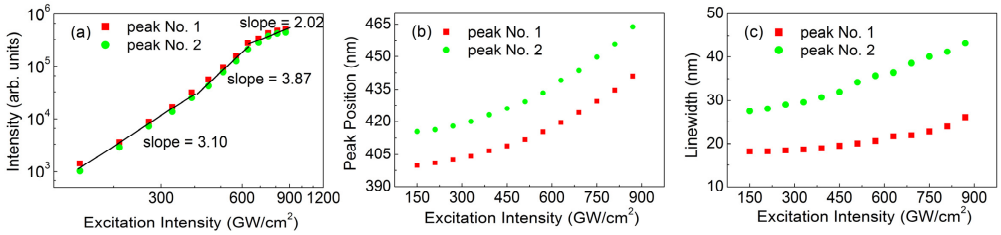

Fig. 11. Excitation intensity dependence of the luminescence peak intensity (a), peak wavelength (b) and bandwidth (c) for the first two emissions originating from the free excitons and Zn_i.

Since the emission band is narrow, we can clearly identify the redshift of the emission band with increasing excitation intensity. On the other hand, the redshift appears to be continuous. These two features remind us that the redshift may originate from the significant increase in the temperature of the ZnO NRs induced by the focused fs laser with a high repetition rate. This assignment is supported by the evolution of the peak wavelength for the two emission bands shown in Fig. 11(b). It is noticed that the separation between the two peaks, which represents the ionization energy of Zn_i, remains nearly unchanged with increasing excitation intensity. In Fig. 11(c), a broadening of the bandwidth with increasing excitation intensity and thus temperature is observed for both emission bands and it appears to be more significant for the second one. It is thought that both the homogeneous broadening originating from the increase in temperature and the state filling effect due to high carrier densities are responsible for the broadening of the bandwidth.

#250796 Received 28 Sep 2015; revised 26 Oct 2015; accepted 27 Oct 2015; published 30 Oct 2015
© 2015 OSA

3.6 Heat accumulation effect

Previously, a systematic study on the melting behavior of Au NRs revealed that the excitation intensity necessary to melt Au NRs dispersed in a PVA film is larger when an objective lens with a larger numerical aperture (NA) is used because of the heat accumulation effect [44]. For an objective lens with a large NA, the focal volume is small and so is the number of Au NRs (heat sources) included in the focal volume. On the other hand, the heat accumulation in this case is not significant because of the large ratio of surface area to volume. As a result, a higher excitation intensity is required in order to reach the melting point of Au NRs. This abnormal phenomenon is confirmed both numerically and experimentally [44]. In our case, the densely-packed ZnO NRs that form flowers are distributed in air whose thermal conductivity is even smaller than that of PVA. Thus, the heat accumulation induced by fs laser light should be more significant, leading to a high temperature in the ZnO NRs. The evolution of the bandgap energy of ZnO with increasing temperature is calculated based on the relationship given in the previous literature [45,46]. It shows that the emission wavelength corresponding to the band edge recombination of ZnO can be shifted to ~440 nm if the temperature of ZnO is raised to ~1100 K. This temperature can be easily achieved by using a focused fs laser light with a high repetition rate to excite densely packed ZnO NRs.

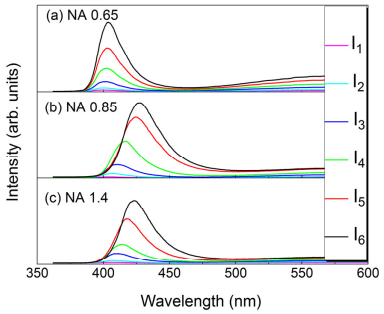

Fig. 12. Evolution of the emission spectrum of the ZnO NRs with increasing excitation intensity observed by using objective lenses with different NAs. (a) NA = 0.65, I_1 = 35 GW/cm^2, I_2 = 58 GW/cm^2, I_3 = 81 GW/cm^2, I_4 = 104 GW/cm^2, I_5 = 127 GW/cm^2, I_6 = 150 GW/cm^2, (b) NA = 0.85, I_1 = 138 GW/cm^2, I_2 = 231 GW/cm^2, I_3 = 323 GW/cm^2, I_4 = 415 GW/cm^2, I_5 = 508 GW/cm^2, I_6 = 600 GW/cm^2 and (c) NA = 1.4, I_1 = 550 GW/cm^2, I_2 = 917 GW/cm^2, I_3 = 1284 GW/cm^2, I_4 = 1651 GW/cm^2, I_5 = 2018 GW/cm^2, I_6 = 2385 GW/cm^2.

In order to confirm the effect of heat accumulation, we have measured the excitation-intensity-dependent MPL of the ZnO NRs by using objective lenses with different NAs and the results obtained at an excitation wavelength of 750 nm are compared in Fig. 12. The NAs for the objective lenses are 0.65, 0.85, and 1.40 and the corresponding excitation spot sizes are estimated to be 4.0, 2.0, and 1.0 μm in diameter, respectively. It was found that the largest redshift of the luminescence peak was achieved when the objective lens with NA = 0.85 was used. In this case, the peak wavelength was redshifted to ~428 nm at an excitation intensity of 600 GW/cm^2. Basically, the temperature rise in the ZnO NRs is induced by the coupling between carriers and phonons. It is determined not only by the carrier density generated in the Zn NRs but also on the heat diffusion which is related to the gradient of temperature and the thermal conductivity of the material surrounding the heat source. Under the same excitation power, the largest excitation intensity and thus the carrier density is obtained by using the objective lens with NA = 1.4 because of the small excitation spot. However, the heat diffusion is also fast because only a few Zn NRs included into the focal volume are heated. In comparison, the use of the objective lens with NA = 0.65 leads to the smallest carrier density but an effective heat accumulation because of the larger excitation spot. A balance between the carrier density and the heat accumulation is achieved by using the objective lens with NA = 0.85. Consequently, the ZnO NRs located at the center of the focal volume can be heated to a higher temperature, resulting in the largest redshift observed in the experiments. The strong dependence of the redshift on the NA of the objective lens clearly indicates that it is the

#250796 Received 28 Sep 2015; revised 26 Oct 2015; accepted 27 Oct 2015; published 30 Oct 2015
© 2015 OSA

temperature rise in the focal volume caused by the heat accumulation effect dominates the redshift of the MPL. It should be emphasized that the heat accumulation effect and high temperature are not expected for ZnO film or ZnO microstructures because the thermal conductivity of ZnO is much better than air and the heat diffusion is efficient.

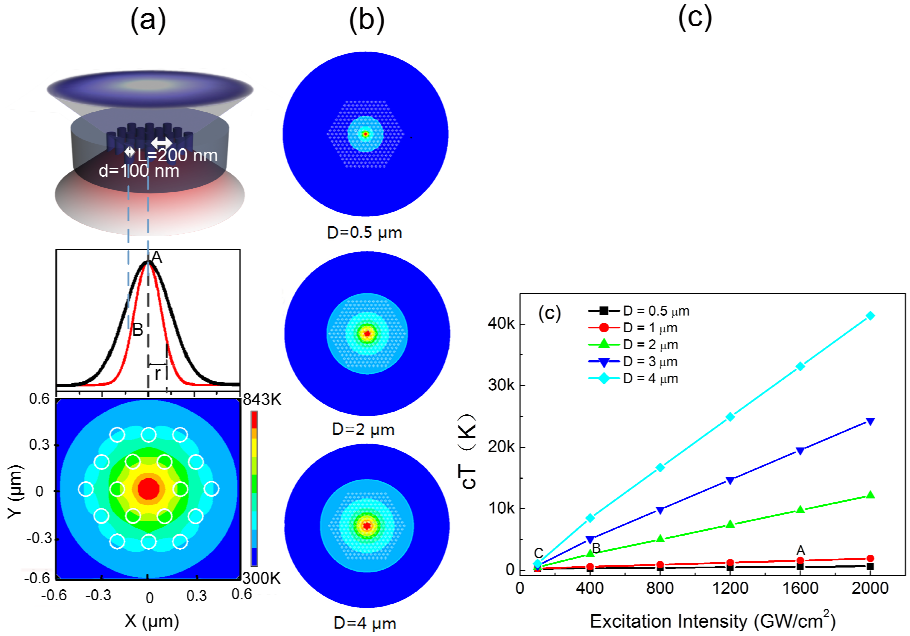

Fig. 13. (a) Schematic showing the closely packed ZnO NR and the one- and two-dimensional intensity distribution of the focused laser beam. (b) Calculated temperature distributions for the array of ZnO NRs induced by the focused laser beams with different diameters of D = 0.5, 2, and 4 μm. (c) Dependence of the maximum temperature achieved in the array of ZnO NRs on the excitation intensity calculated for the focused laser beams with different diameters.

The heat accumulation effect occurring in the ZnO NRs excited by fs laser light with different excitation spot sizes has been simulated by solving the thermal diffusion equation. In the simulation, we compared several cases in which the diameters of the excitation spots were set to be D = 0.5, 1, 2, 3, and 4 μm after considering the cubic dependence of the three-photon absorption (3PA) on the intensity of the incident light. The length and diameter of the ZnO NRs were chosen to be 2 μm and 100 nm. The ZnO NRs were assumed to be arranged into a hexagonal lattice with a lattice constant of L = 200 nm in the focal volume, as shown in Fig. 13(a). Each ZnO NR in the focal volume acts as a heat source with released heat energy proportional to the 3PA and thus the cubic of the local light intensity. The thermal conductivity of air was chosen to be 0.0317W/m·K [47]. Since we do not know the absorption coefficient of 3PA and the efficiency of optical-thermal conversion after 3PA, a constant c was used in the numerical simulation and only a relative temperature (cT) was obtained. The temperature distributions obtained for three excitation spot sizes are presented in Fig. 13(b) where one can identify the heat accumulation effect from the highest temperature achieved at the center of the focal spot. In Fig. 13(c), we present the highest temperature achieved at the center of the focal spot with increasing excitation intensity calculated for different excitation spot sizes ranging from 0.5 to 4 μm. It can be seen that a larger slope is observed when a larger excitation spot is employed, implying the existence of significant heat accumulation effect. Therefore, the maximum temperature achieved in the array of ZnO NRs depends not only on the excitation intensity but also the excitation spot size. In Fig. 13(c), we indicate the maximum temperatures achieved in the array of ZnO NRs by using three excitation spot diameters of 4, 2, and 1 μm, which correspond approximately to those achieved by using the objective lenses with NAs of 0.65, 0.85, and 1.40, respectively. It

#250796 Received 28 Sep 2015; revised 26 Oct 2015; accepted 27 Oct 2015; published 30 Oct 2015
© 2015 OSA

can be seen that the simulations results are qualitatively agreement with the experimental observations presented in Fig. 12, indicating that the heat accumulation effect plays a crucial role in achieving the blue emission from the ZnO NRs.

3.7 Physical mechanism for the 3PL of the ZnO NRs

From the excitation-intensity-dependent MPL shown in Fig. 11(a), we can easily determine a slope of ~3.10 for both emission bands, implying that 3PA is involved. As far as 3PA processes are concerned, there are three possible ways. One is the one-photon excitation to a real energy level followed by a 2PA. Another is the two-photon simultaneous excitation to a real energy level followed by one-photon absorption (1PA). The third is the three-photon simultaneous absorption. The first case can be ruled out due to the absence of the absorption in the wavelength range of 750–800 nm. In general, the transition probability of an electron to a real energy level is much larger than that to a virtual level with the same energy. Thus, the possibility for the three-photon simultaneous absorption is quite small. Therefore, the second case is considered as the dominant process in generating 3PL.

Now we need to explain why the excitation-intensity-dependent 3PL exhibits different slopes in different excitation regimes. At low excitation intensities, the slope is estimated to be ~3.10, implying that 3PA is the dominant process. In the moderate excitation intensities, the slope becomes larger (~3.87) because of two reasons. First, the reduction of bandgap energy due to the increase in temperature leads to the excitation of carriers in high-energy states, creating more carriers. Second, more carriers are captured into the defect levels related to Zn_i in the competition between the defect levels of Zn_i and those of O vacancies, resulting in a rapid increase in the blue emission and the saturation of the green emission (see Fig. 10). At high excitation intensities, the coupling between carriers and photons will become stronger and more carriers will recombine nonradiatively by transferring their energies to phonons, resulting in a smaller slope of ~2.02.

4. Conclusion

In summary, we have synthesized flower-like ZnO NRs by using the hydrothermal method. The formation of Zn_i was confirmed and the concentration of Zn_i was found to increase with increasing synthesis temperature. A strong blue emission band with a narrow bandwidth of ~30 nm was observed when irradiating the ZnO NRs with focused fs laser light at 750 nm. It was revealed that the bandgap renormalization induced by the large concentration of Zn_i and the heat accumulation effect caused by the close packing of ZnO NRs are responsible for the blue emission observed at high excitation intensities. The flower-like ZnO NRs like this and the efficient blue emission produced by using the excitation scheme proposed in this work may find applications in the fields of optical display, high-temperature sensors and light therapy of tumors.

Acknowledgments

The authors acknowledge the financial support from the National Natural Science Foundation of China (NSFC) (Grant Nos. 51171066, 11374109 and 61475038).

#250796 Received 28 Sep 2015; revised 26 Oct 2015; accepted 27 Oct 2015; published 30 Oct 2015
© 2015 OSA